2013

Elevated Electron Temperatures Around Twin Sporadic E Layers at Low Latitude: Observations and the Case for a Plausible Link to Currents Parallel to the Geomagnetic Field

A. Barjatya
Embry-Riddle Aeronautical University, barjatya@erau.edu

J. P. St. Maurice
University of Saskatchewan

C. M. Swenson
Utah State University

Scholarly Commons Citation

Barjatya, A., J.-P. St-Maurice, and C. M. Swenson (2013), Elevated electron temperatures around twin sporadic E layers at low latitude: Observations and the case for a plausible link to currents parallel to the geomagnetic field, J. Geophys. Res. Space Physics, 118, 7316–7328, doi:10.1002/2013JA018788

JOURNAL OF GEOPHYSICAL RESEARCH: SPACE PHYSICS, VOL. 118, 7316–7328, doi:10.1002/2013JA018788, 2013

Elevated electron temperatures around twin sporadic *E* layers at low latitude: Observations and the case for a plausible link to currents parallel to the geomagnetic field

A. Barjatya,[1] J.-P. St-Maurice,[2] and C. M. Swenson[3]

Received 6 March 2013; revised 14 October 2013; accepted 15 October 2013; published 11 November 2013.

[1] We present data from nighttime sounding rocket flights in the low latitude *E* region. The payloads carried a sweeping Langmuir probe, a plasma impedance probe, and electric field probes. A detailed examination of the plasma density, temperature, and electric field measurements show two strong sporadic *E* (E_s) layers with very high electron temperatures (∼1000 K) on each side of the upper layer. The lower layer was consistent with the presence of a strong zonal neutral wind shear. The upper layer was strongly influenced by the presence of a strongly negative vertical electric field, with zonal winds and their shears also contributing. A strong downward motion of the plasma from the combined action of the downward electric field and negative zonal wind advected the upper layer far below the region of maximum growth. We have attributed the more puzzling high electron temperatures to frictional heating from parallel currents and shown that the *F* region nighttime dynamo could easily generate the necessary parallel current densities (1 μA m^{-2}) near the electron density troughs. The electron temperature was also elevated in the E_s layers themselves, implying parallel current densities of the order of 15 μA m^{-2} around the E_s peaks. Those parallel currents were attributed to strong Hall current divergences driven by the zonal electric field around the E_s peaks.

Citation: Barjatya, A., J.-P. St-Maurice, and C. M. Swenson (2013), Elevated electron temperatures around twin sporadic *E* layers at low latitude: Observations and the case for a plausible link to currents parallel to the geomagnetic field, *J. Geophys. Res. Space Physics*, *118*, 7316–7328, doi:10.1002/2013JA018788.

1. Introduction

[2] The *E* region ionosphere is accessible indirectly through radars or directly through rocket flights. The smallest scale structures tend to be turbulent and are characterized as "irregularities." Those irregularities are often triggered by larger-scale structures that are more organized, like sporadic *E* (E_s) layers. Away from the high-latitude regions, the electric fields of electrodynamical structures are usually generated by neutral winds. Thus, there is great interest in studying the *E* region with as many instruments as possible to assess not just how E_s layers form but also how they generate irregularities and how they couple to the *F* region, higher up. In addition, some observations of electron temperature structures in the *E* region have until now not been explained, and we argue below that these features are related to electrodynamics. This, in turn, has implications for our understanding of the coupling between various ionospheric regions.

[3] Langmuir probes have been the most widely used in situ instruments for rocket-based measurements of plasma parameters such as electron density (n_e), temperature (T_e), ion density (n_i), and as an indicator for spacecraft charging [*Chen*, 1965; *Brace*, 1998; *Barjatya et al.*, 2009]. Although the technique itself is simple and straightforward, the accuracy of derived plasma parameters is key to establishing a basic understanding of *E* region processes. The accuracy is determined by the applicability of the theory used to analyze the data and the engineering quality of the probe.

[4] Of all the Langmuir probe design constraints, the hardest challenge in a sounding rocket payload is to ensure a favorable surface-to-probe area ratio. The probe, the plasma, and the spacecraft chassis ground create a closed current loop. As a result, the surface area of the spacecraft has to be much larger than that of the Langmuir probe operating in the electron saturation region to provide for return ion currents to the plasma. If the area ratio of spacecraft surface to probe surface is not of the order of 1000 or greater, the spacecraft floating potential can become highly negative and attract significantly more ions to balance the electron current collected by the probe [*Szuszczewicz*, 1972]. Due to the

[1]Physical Sciences Department, Embry-Riddle Aeronautical University, Daytona Beach, Florida, USA.
[2]Department of Physics and Engineering Physics, University of Saskatchewan, Saskatoon, Saskatchewan, Canada.
[3]Electrical Engineering Department, Utah State University, Logan, Utah, USA.

Corresponding author: A. Barjatya, Physical Sciences Department, Embry-Riddle Aeronautical University, 600 S. Clyde Morris Blvd, Daytona Beach, FL 32114 USA. (barjatya@erau.edu)

2169-9380/13/10.1002/2013JA018788

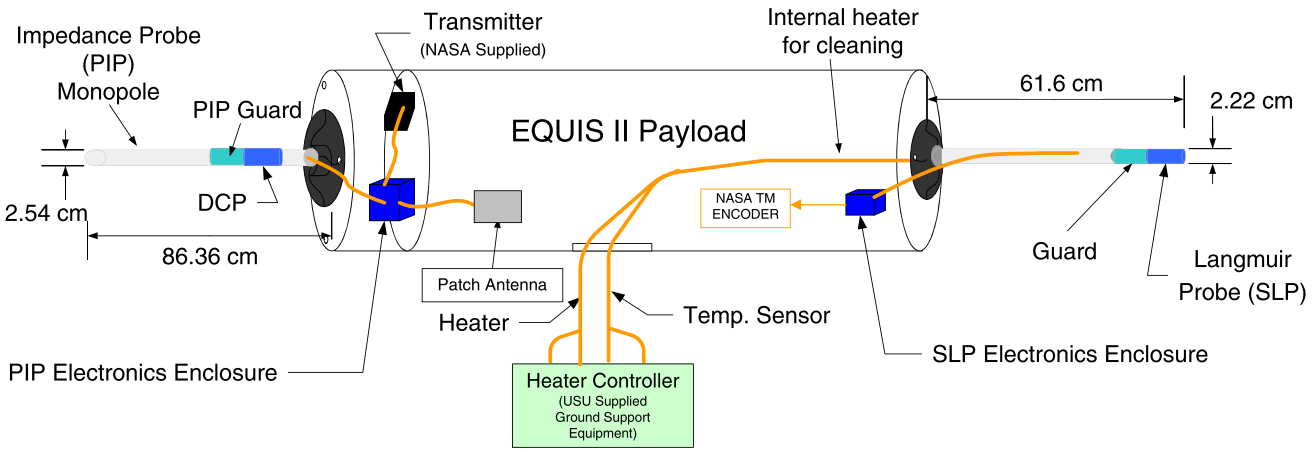

Figure 1. The EQUIS II payload schematic showing various instruments.

small payload skin area on a typical sounding rocket, the probe can therefore not be large. A small Langmuir probe in turn limits the magnitude of current collection, thereby imposing strong requirements on the sensitivity and noise floor of the electronics.

[5] A first aim of the present paper is to describe the data analysis of sweeping Langmuir probes flown aboard two separate sounding rocket payloads, where the ratio of the Langmuir probe area to that of the payload skin was about 250. We not only derive electron density and temperature from the Langmuir probe *I-V* curves but also cross-check the derived plasma density with another instrument that is immune to spacecraft charging effects. The crucial point of this data analysis presentation is to establish the validity of our observations, as well as set a stage for further usage of these instruments in future rocket missions. We then turn to the observations themselves in the second part of this paper. The observations include high-resolution measurements of clear and unambiguous electron density and temperature anticorrelations around a region with two sporadic E_s layers, with electron temperatures reaching up to 1000 K in the density troughs. We discuss the origin of the layers in terms of the observed electric fields and neutral winds and delve into the question of the origin of the elevated electron temperatures which we argue can only be attributed to electron-borne currents flowing along the geomagnetic field. The origin of these currents is then discussed in terms of the various plasma parameters that were observed.

2. Experiment Background and Instrument Description

[6] The rocket investigation "Scattering Layer in the Bottomside Equatorial *F* region Ionosphere" was part of the NASA EQUIS II campaign [*Hysell et al.*, 2005]. It was an investigation of the electrodynamics of the post-sunset equatorial *F* region ionosphere and the bearing it has on the development of thin radar scattering layers that are observed in the bottomside of the *F* region ionosphere. These thin layers appear to be a precursor to equatorial spread-*F* and are difficult to study with satellites due to their occurrence at low altitudes. The EQUIS II campaign was the first sounding rocket investigation of these layers. Two salvos of sounding rockets were launched from Roi Namur in Kwajalein atoll on 7 and 15 August 2004. Each of the salvos consisted of one instrumented and two chemical release payloads. The instrumented rockets were launched westward into an equatorial spread-*F* precursor that was first observed from the ground using the Altair radar. The instrumented rockets reached an apogee of about 420 km. The instruments consisted of a Sweeping Langmuir Probe (SLP), a fixed-bias DC Langmuir Probe (DCP), and a Plasma Impedance Probe (PIP). The payload also carried four floating spheres as part of an Electric Field Probe (EFP) instrument.

[7] Figure 1 shows a schematic of the payload in relation to some of its instruments. The PIP boom was 86.36 cm long, 2.54 cm thick, and built out of aluminum. Of the total boom length, the last 50.48 cm were used as the monopole PIP antenna, making it electrically short for frequencies below 600 MHz. The PIP instrument was used to lock-on and track the upper hybrid resonance of plasma with a phase-locked loop at a time resolution of 0.28 ms and a frequency resolution of 1 KHz. The knowledge of the upper hybrid resonance coupled with cyclotron frequency derived from International Geomagnetic Reference Field model results in very accurate absolute electron density measurement.

[8] The DCP was a 5.08 cm long cylinder located at the base of the PIP boom. It was driven at +3 V relative to the payload chassis ground to operate it in the electron saturation region. In order to keep the ion sheath around the DCP from interfering with the operation of the PIP (PIP being the higher priority instrument), the PIP was separated from the DCP by a 7.93 cm long cylinder that was electrically isolated from the PIP but operated at the same frequencies as the PIP.

[9] The SLP was built out of aluminum with a length of 6 cm and a diameter of 2.22 cm. It was guarded on one side with an element of the same dimensions and at the same potential as the SLP. The combined probe and guard assembly was at the end of a 61.6 cm boom. With the exception of the probe and the guard, the rest of the boom was coated with a nonconductive paint. The SLP was internally heated via a cartridge heater for several hours before launch at 150°*C* to boil off surface contamination and was launched hot. The probe was swept in 549 equal steps from –1 to +5 V relative to the payload chassis ground in a triangular waveform pattern at 25 Hz, giving 50 *I-V*

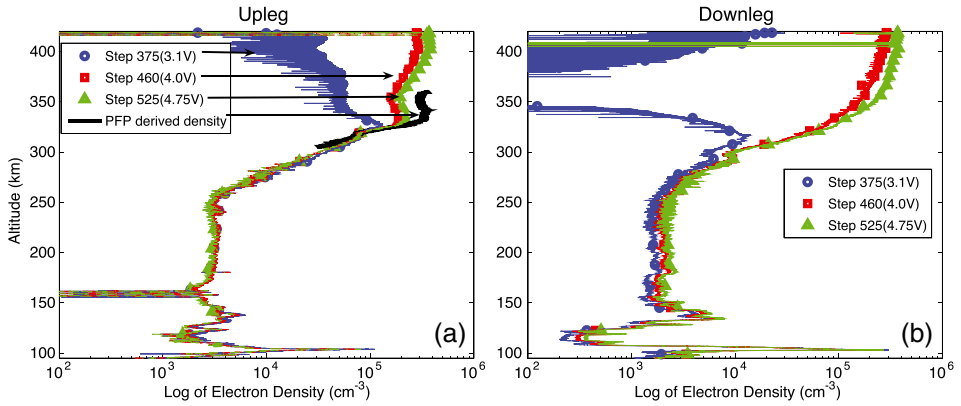

Figure 2. Quasi-DC plot of the SLP data to derive relative density profile. On the upleg, where the PFP locked, the absolute density from the PFP does not match the Quasi-DC density except at the point of normalization at 305 km.

curves every second. The instrument used 16 bit analog to digital converters (ADC) and measured the current in two different channels: the High-Gain channel at a resolution of 57.9 pA/count with a range of ±1.897 μA and the Low-Gain channel at a resolution of 5.85 nA/count with a range of ±191.6 μA. The SLP was meticulously calibrated in a thermal-vacuum chamber over a range of resistor loads and temperatures. The load values were chosen so as to exercise each of the gain channels through their entire dynamic range of operation. A description of the meticulous calibration process is presented in *Barjatya* [2007]. The internal instrument noise was within a few counts of the ADC for each channel.

[10] The rocket actively controlled its attitude to align the spin axis (the payload long axis) parallel to the magnetic field, while the rocket trajectory was nearly perpendicular to the magnetic field. Thus, the SLP and the PIP sensors were never in the payload wake with the booms perpendicular to the ram direction and parallel to Earth's magnetic field. Although not shown in Figure 1, the electric field double probe (EFP) instrument used four spheres deployed radially out from the payload on booms.

3. Data Analysis

[11] The PIP acquired a lock on the plasma upper hybrid resonance for several tens of seconds but only in the upleg portion of both the rocket flights. Thus, it only provided absolute electron density for several tens of kilometers in the *F* region ionosphere and not throughout the two flights. A widely used method to acquire density measurement for the entire flight duration is to normalize the fixed bias Langmuir probe (DCP) data to the absolute density data derived from other instruments such as PIP in our case, thereby providing high resolution density measurements [*Friedrich et al.*, 2013; *Barjatya and Swenson*, 2006]. But for these two rocket payloads, data from the DCP at the base of the PIP was influenced by the oscillations in the payload chassis ground as well as ion sheath resonance effects from the PIP, and thus the DCP data are not suitable for use as a density measurement and are not presented here.

[12] Another quasi-DC measurement made over the entire flight comes from the SLP by considering only a constant voltage step from the total voltage sweep. In other words, the SLP can be considered as several fixed-bias DCPs operating sequentially at different voltages. The quasi-DC data can then be normalized to the PIP-derived absolute density to get the density profile for the entire flight. Figure 2 shows the 15 August flight's (29.037) quasi-DC data at several different voltage steps normalized to the PIP lock derived density at 305 km altitude. Similar to the DCP that was biased at +3 V, the +3.1 V quasi-DC data from SLP is heavily influenced by negative payload charging in *F* region. For higher quasi-DC voltages, the effect seems to be less drastic, as the normalized density below 300 km seems to be constant between different voltages (which is exactly the intended fixed-bias Langmuir probe operation employed on sounding rockets). However, it is critically important to note that the quasi-DC derived relative density profile does not exactly match the PIP derived absolute density except at the very point of normalization. Similar observations on multiple flights have also been reported by *Bekkeng et al.* [2013].

[13] The premise of a fixed bias DC Langmuir probe's operation is that the electron saturation current is directly proportional to density, and that the measurement is made at the same potential relative to plasma potential. In actuality, the probe is applied a potential relative to the payload chassis ground. Our observations in Figure 2 caution toward the accuracy of the DCP method of relative density measurement that is used frequently on rocket flights. The caution arises due to two reasons. First, in a typical rocket flight, the plasma temperature can change by an order of magnitude within the 100–400 km altitude range. This changes the floating potential of the payload and thereby the Langmuir probe potential relative to plasma. Thus, the current collected by the DCP is no longer influenced just by changing density but also by the changing floating potential which is affected by changing plasma temperature. Second, any additional current source to the payload-probe system, such as electron collection by exposed potentials or triboelectric current collection [*Barjatya and Swenson*, 2006], will change the payload floating potential. Thus, the technique of high spatial resolution density measurements using fixed-bias Langmuir probe data after normalization to absolute density measurements can be prone to significant errors that are dependent upon the stability of the payload chassis

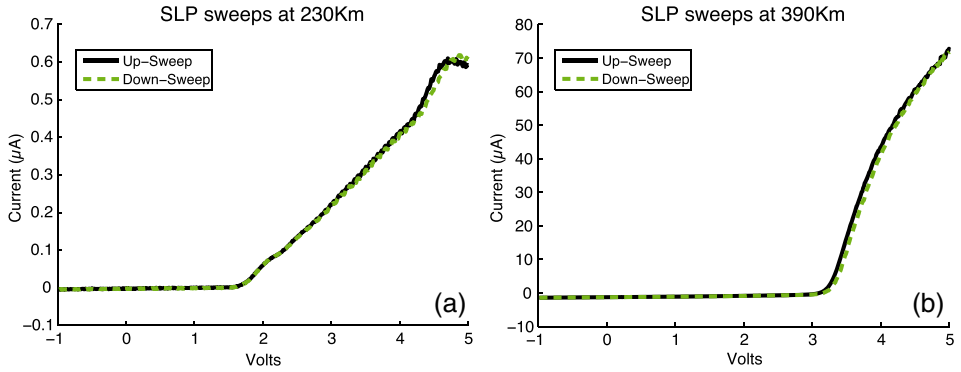

Figure 3. (a) Typical SLP upsweep and downsweep observed on both flights at low altitudes (<250 km). The current shows a "negative" characteristic and drops with applied higher voltages. (b) Two consecutive SLP sweeps, at an altitude of 390 km showing negligible hysteresis.

ground relative to the plasma. Note that these errors are in addition to what one might get when the fixed bias probe surface is contaminated [*Steigies and Barjatya*, 2012].

[14] Of further concern is a "negative" characteristic observed in the electron saturation region of the SLP *I-V* curves as shown in Figure 3a. This phenomenon was observed only in the lower altitude region *I-V* curves. It is present in both the upleg and downleg trajectories for both of the rocket flights. It has also been seen intermittently on a cylindrical Langmuir probe aboard the International Space Station [*Barjatya et al.*, 2009]. This phenomenon occurs at the very top of our voltage sweep and thus makes suspect any DCP type relative density data obtained with large fixed-bias voltages. An explanation and analysis of this feature of the *I-V* curve will be the topic of a future paper. Another problem in a sweeping Langmuir probe implementation is the presence of hysteresis in consecutive up and down sweeps. This is attributed to the contamination of the probe surface. Figure 3b presents two consecutive SLP sweeps from 390 km. The lack of any significant hysteresis, in both the lower altitude and the higher altitude sweeps, can be attributed to the internally heated probe [*Amatucci et al.*, 2001] as well as fast 25 Hz sweeping [*Oyama*, 1976; *Oyama et al.*, 2008a]. Heating is expected to remove the contamination and the fast sweeping is expected to short circuit the contamination capacitance.

[15] In the absence of a PIP lock on the upper hybrid resonance that lasts throughout the rocket flight, the only option that remains to derive accurate absolute density profiles is to use the SLP *I-V* curves. As the payload surface-to-probe area is not sufficiently large, when the SLP sweeps far into the electron saturation region and collects large electron current, it drives the payload chassis potential negative with respect to the plasma potential. Thus, the electron saturation region is expected to be corrupted by the "warping" of the *I-V* curve due to payload surface charging. Furthermore, as mentioned in section 1, to date there has been no theory developed that can address saturation current collection by any typical probe geometry in a magnetized mesothermal collisional plasma. *Barjatya et al.* [2009] presented a technique wherein they curve fit the analytical expression of the Orbital Motion Limited (OML) theory to the electron saturation region to derive the electron density. For the sounding rocket, as the payload to probe surface area is small, we instead curve fit to the electron retardation region and ion saturation region. The current collection in electron retardation region is geometry independent, and the current collection in ion saturation region does not lead to swings in payload potential. Our multistep procedure to derive absolute ion density from the EQUIS II payload *I-V* curves is explained next.

[16] In the first step, subtraction of a line fit to the ion saturation region from the total collected current approximately gives the electron collection current, I_e. The location of the $dI_e/d\phi$ maxima within 2 eV of the floating potential (ϕ_f) gives a first-order approximation to the plasma potential (ϕ_p). The value of ϕ_f is determined by the point where the total collected current goes to zero. By equating the value of the ion saturation current linear fit at the location of ϕ_p to ion ram collection current, we get a first-order approximation to the ion density.

[17] In the second step, we assume the plasma to be quasi-neutral ($n_i = n_e$) and do a nonlinear least squares fit of the total collected current to

$$I_{\text{total}}(\phi) = -n_i e A_{\text{ram}} V_{\text{ram}} + n_e e A \sqrt{\frac{k_B T_e}{2\pi m_e}} \exp\left(\frac{e(\phi - \phi_p)}{k_B T_e}\right), \quad (1)$$

where the first term is the ion ram current and the second term the electron retardation current. We use the density as calculated in the first step and fit equation (1) in a least squares sense for only T_e and ϕ_p. The nonlinear fit is done only for points within $\phi_f - 0.05$ eV to $\phi_f + 0.02$ eV. This nonlinear fit gives a more accurate value of ϕ_p than that derived in the first step. The fit is done on a limited range of points because the farther we go in the electron retardation region (and eventually into saturation region), the more the payload floating potential is expected to charge negative due to insufficient ion collection from the payload surface to counter the increasing electron current collection.

[18] In the third step, we fit the ion saturation current region of the *I-V* curve to

$$I_{\text{total}}(\phi) = -n_i e A \sqrt{\frac{k_B T_e}{2\pi m_i}} \left(1 - \frac{e(\phi - \phi_p)}{k_B T_e}\right)^{\beta}. \quad (2)$$

in a least squares sense for n_i and β, while using T_e and ϕ_p as derived in second step.

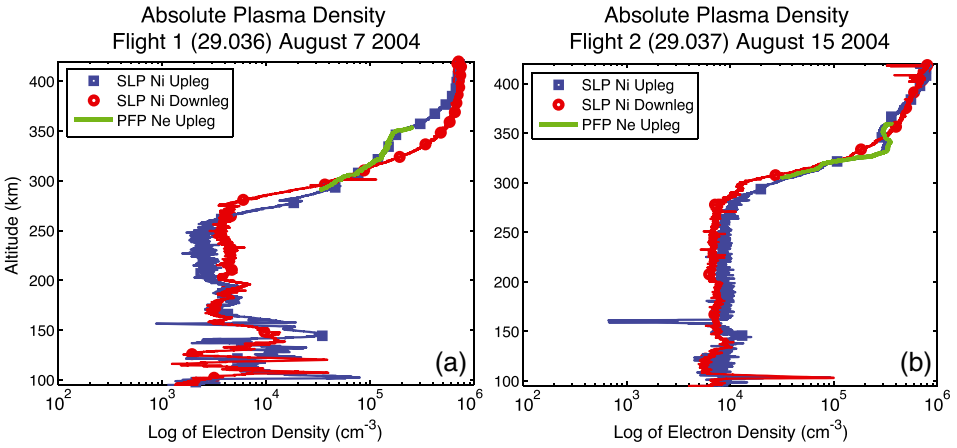

Figure 4. Plasma density for both the EQUIS II (29.036 and 29.037) rocket flights. Note that the PFP-derived absolute density is a much better match with the SLP-derived absolute density throughout the altitudes where PFP had a lock.

[19] In the fourth step, with the improved value of n_i and the fit value of β, we do another least squares fit for points within $\phi_f - 0.05$ eV to $\phi_f + 0.05$ eV to

$$I_{\text{total}}(\phi) = -n_i e A_{\text{ram}} V_{\text{ram}} + n_e e A \sqrt{\frac{k_B T_e}{2\pi m_e}} \exp\left(\frac{e(\phi - \phi_p)}{k_B T_e}\right) - n_i e A \sqrt{\frac{k_B T_e}{2\pi m_i}} \left(1 - \frac{e(\phi - \phi_p)}{k_B T_e}\right)^{\beta}. \quad (3)$$

This is similar to the second step, but the inclusion of the OML-type ion saturation current expression gives a better fit for T_e and ϕ_p. Finally, in the fifth step, we use the latest fit values of T_e and ϕ_p to recalculate step three and get the final value of n_i. We stop the iterations when the squared norm of the residual after the least squares curve fit is smaller than 1E-17 for fits to T_e and smaller than 1.5E-16 for fits to n_i. The number of iterations needed usually depends on the curve. If plasma density is low and therefore the signal to noise ratio is low, more iterations may be required, as opposed to when there is plenty of ionization and the curve is smoother. Nevertheless, we found that two to three iterations were sufficient most of the time and any further iterations changed the values of derived parameters by less than 1%. The case may be different for another mission and another instrument. The results of this multi-step iterative procedure to derive density and temperature are shown in Figures 4 and 5.

[20] The absolute density derived from the SLP *I-V* curves using the above multistep procedure matches the PIP-derived density for the entire duration the PIP had a lock on the plasma upper hybrid frequency. However, the density resolution at lower altitudes suffers due to lower sensitivity of the SLP to ion current. The "bumps" in the temperature profile above 250 km in both upleg and downleg trajectories of the 29.037 rocket are not expected and not completely explicable. They coincide with a strong shear flow of about 190 m/s observed through the E field data [*Hysell et al.*, 2005]. In this paper we focus on another temperature feature found lower down in the *E* region, where a density-temperature anticorrelation was observed in association with a pair of E_s layers, shown in Figure 6a. It is not reasonable to estimate the nuanced accuracy of the OML theory used to derive the plasma parameters for our specific probe configuration. However, we can estimate the error bars caused by the noise in the instrument. We simulate the OML expressions in a SPICE model [*Barjatya and Swenson*, 2006; *Barjatya*, 2007] using precise payload and probe surface

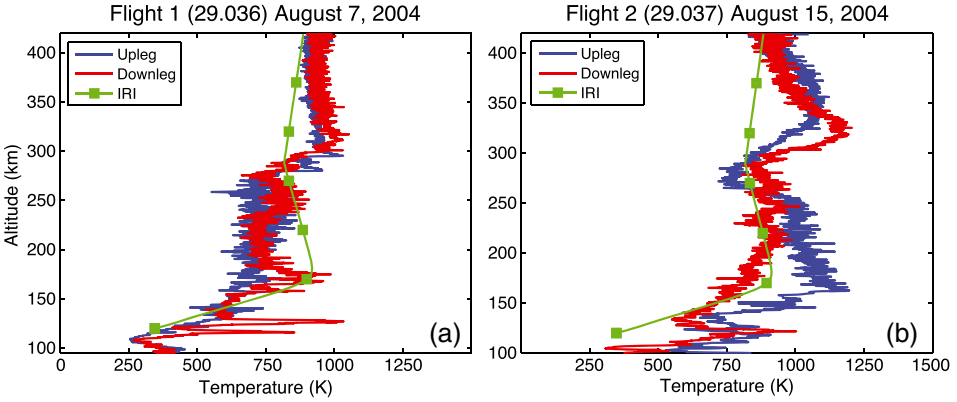

Figure 5. Plasma temperatures for both the EQUIS II (29.036 and 29.037) rocket flights.

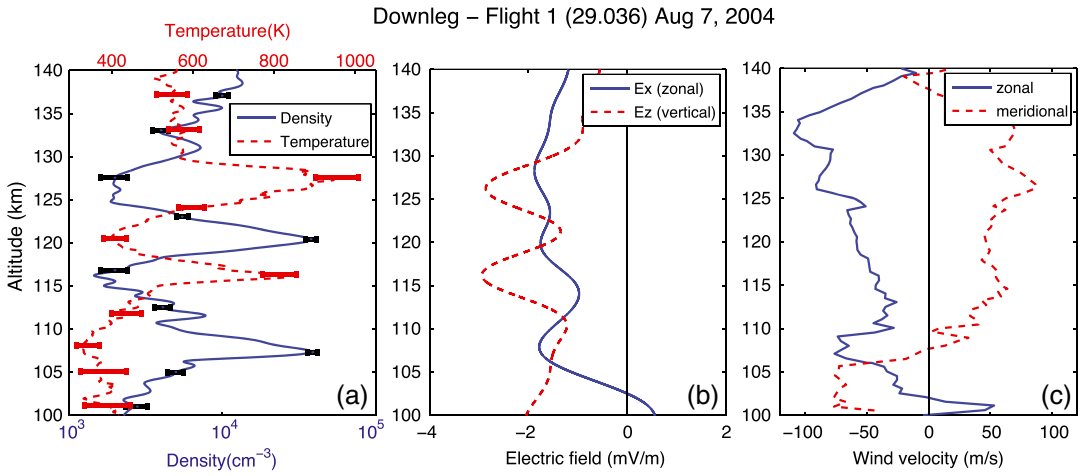

Figure 6. (a) Anticorrelation in density and temperature observed within and around double sporadic *E* layer on the downleg of 29.036 rocket flight. Also shown are in situ measured (b) *E* fields and (c) wind profiles derived from a TMA release experiment.

area dimensions. This generates the periodic "warping" of the *I-V* curve due to payload surface charging. We then introduce white noise into the simulated *I-V* curve equivalent to 3 bits of noise that was present in the instrument analog to digital converter. Such *I-V* curves are created for various combinations of N_e and T_e. We then use the iterative method as described above to back out the plasma parameters that were used to generate the curves in first place. Based on our results, we can now include error bars on N_e and T_e as shown in Figure 6a. The error bars are small for regions of high plasma density due to high signal-to-noise ratio. It is also worth noting that the graph is logarithmic in the *x* axis.

4. E_s Layer Formation and the Meaning of the Electron Density-Temperature Anticorrelation

[21] The key features addressed in the rest of this paper are presented in Figure 6, obtained during the 29.036 rocket flight. Figure 6a shows how the *E* region electron density and temperatures were clearly anticorrelated, with the electron temperature going through two peaks with values well above the normal background temperature. The zonal and vertical electric field components are shown in Figure 6b, with a particularly clear undulation seen in the vertical component of the electric field and the altitude of the vertical electric field minima nicely matching the heights of the electron temperature peaks. The zonal and meridional components of the neutral wind—which were already presented in *Hysell et al.* [2006]—are shown in Figure 6c with strong shears in both components around 107 km altitude, right around where the lower E_s layer was found.

[22] Electron temperature enhancements around E_s layers have actually been reported before [e.g., *Oyama et al.*, 2008b, and references therein]. One difference here is that our data are of a higher spatial resolution and include the zonal and vertical electric field and wind measurements. Such data allow us to not just query the origin of the pair of E_s layers but also track the origin of the hot electrons. This is done in the next subsections. We propose a mechanism for the elevated electron temperatures that is based on the notion of frictional heating produced by thermal electron drifting along the magnetic field. From this we have computed the magnitude of the electron drifts involved and infer the associated magnitude of the parallel current densities and parallel electric fields. The parallel current densities thus inferred seem to be consistent with the presence of the observed combination of sharp E_s layers and accompanying deep troughs that were subject to the influence of the nighttime electric fields that were observed.

4.1. E_s Layer Formation

[23] Normally, one would expect that zonal wind shears are responsible for the production of E_s layers below 130 km (see *Haldoupis et al.* [2004] and references therein for a thorough discussion). However, in the present case, a relatively strong electric field was also present. As we show here, this field was actually strong enough to compete with the neutral wind for the production of a vertical ion drift and its attendant divergence.

[24] We start with the vertical ion drift: as is well-known, after just a few ion-neutral collision times (1 s or less in the *E* region), the response of the ions to a neutral wind and an electric field is given by the steady state solution

$$\mathbf{V}_i = \frac{1}{\alpha}\frac{\mathbf{E}_\parallel}{B} + \frac{\alpha}{1+\alpha^2}\frac{\mathbf{E}'_\perp}{B} + \frac{1}{1+\alpha^2}\frac{\mathbf{E}'_\perp \times \mathbf{B}}{B} + \mathbf{V}_n \tag{4}$$

where

$$\alpha = \nu_{in}/\Omega_i \tag{5}$$

$$\mathbf{E}_\perp{}' = \mathbf{E}_\perp + \mathbf{V}_n \times \mathbf{B} \tag{6}$$

[25] We can safely assume that the neutral winds have a negligible vertical component and that parallel electric fields are too small to accelerate the ions along the magnetic field line. In the first of the remaining two terms in equation (4), the zonal component of the electric field and the northward component of the neutral wind do not produce a vertical ion drift, leaving us with the following contribution from the northward/vertical electric field and the zonal wind:

$$V_{iz}^{(1)} = \frac{\alpha}{1+\alpha^2}\frac{E_\perp^{(N)} + V_{nx}B}{B}\cos I \tag{7}$$

where $E_{\perp}^{(N)}$ is the component of the perpendicular field that points to geomagnetic north when a magnetic field line has a nonzero inclination. At low latitudes in the northern hemisphere, this component of the electric field is essentially vertical and defined as positive upward. The x direction is along the zonal direction (positive eastward) and I is the magnetic dip angle (also taken here to be positive).

[26] A second contribution to the vertical ion drift comes from the zonal field, E_x, and the meridional wind, V_{ny}. With the y axis pointing toward magnetic north, this contribution amounts to

$$V_{iz}^{(2)} = \frac{1}{1+\alpha^2}\frac{E_x - V_{ny}B\sin I}{B}\cos I \tag{8}$$

[27] An E_s layer is produced by a convergence of the ion drift. In that context, the continuity equation produces the result

$$\frac{\partial n}{\partial t} + V_{iz}\frac{\partial n}{\partial z} = \frac{Dn}{Dt} = -n\frac{\partial V_{iz}}{\partial z} + P - L = n\gamma + P - L \tag{9}$$

where n is the ion density, V_{iz} is the vertical ion drift, γ is the 'growth rate' of the layer, and P and L are chemical production and loss rates, respectively. We assumed here that the vertical gradients are much steeper than any horizontal gradients. We do not discuss chemistry further here because the layers are observed in the late evening (little or no production) and because it is often observed that the layers contain high concentrations of metallic ions as a result of the ion convergence (weak chemical loss rates).

[28] Using the symbol E_v for $E_{\perp}^{(N)}\cos I$ in the expression for $V_{iz}^{(1)}$, and after taking into account the vertical derivative of α, we obtain for the derivatives of the vertical ion drift the expressions

$$\frac{\partial V_{iz}^{(1)}}{\partial z} = \frac{\alpha}{1+\alpha^2}\frac{\partial}{\partial z}\left[\frac{E_v}{B} + V_{nx}\cos I\right] + \left[\frac{E_v}{B} + V_{nx}\cos I\right]\frac{\alpha}{H_n}\frac{\alpha^2-1}{(1+\alpha^2)^2} \tag{10}$$

and

$$\frac{\partial V_{iz}^{(2)}}{\partial z} = \frac{\cos I}{1+\alpha^2}\frac{\partial}{\partial z}\left[\frac{E_x}{B} - V_{ny}\sin I\right] + \left[\frac{E_x}{B} - V_{ny}\sin I\right]\frac{\cos I}{H_n}\frac{2\alpha^2}{(1+\alpha^2)^2} \tag{11}$$

In these expressions, we have also assumed α to decay exponentially with the neutral scale height H_n, that is, $\partial\alpha/\partial z = -\alpha/H_n$. We note that when the electric field terms are taken out, our two expressions are in agreement with previous midlatitude E_s layer work [*Haldoupis et al.*, 2004]. Our two expressions for the vertical velocity (equations (7) and (8)) have also been used by *Tsunoda* [2008] to study the evolution of daytime E_s layers at low latitudes.

[29] An analysis of the various terms involved in the ion velocity divergence is presented for a typical calculation in Figure 7. This figure shows, first of all, that the meridional wind and zonal field (namely, equation (11); green trace in Figure 7) do not contribute significantly to the growth or decay rates. Partly this is because the second term in equation (11) loses out to the second term in equation (10) for α both large and small. The only exception to this is for the region near $\alpha = 1$. Even then the impact is not strong because the derivatives in the electric field and wind

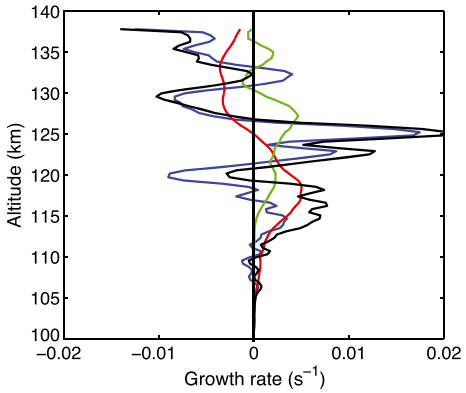

Figure 7. E_s growth rate computation based on the electric field and neutral wind observations. Green trace: total contribution from the zonal field plus meridional winds, namely all the terms in equation (11). Red trace: contribution from the second term in equation (10). Blue trace: total contribution from the first term in equation (10). Black trace: total growth rate.

themselves matter more than the scale height variation. With respect to the latter point, it also turns out that the derivatives in the zonal field are measurably weaker than for the vertical field, which explains the total lack of importance of $V_{iz}^{(2)}$ in creating ion divergence or convergence.

[30] The contribution from the second term in equation (10) is shown by the red trace in Figure 7. As expected from the equation, the sign of this term changes on each side of the $\alpha = 1$ altitude. Though rarely dominant, the magnitude of this term is not negligible. It has fewer undulations than the first term since it does not involve the derivatives of the V_{nx} or E_v. Finally, the first term in equation (10) (blue trace in the figure) can be compared to the total growth/decay rate (black trace) to conclude that it plays a dominant role at all altitudes for which $\alpha \geq 1$. It also significantly modulates the growth/decay rate throughout the altitude region. In this first term contribution, the electric field and zonal wind contributions happen to be approximately the same near the main peak in the growth rate with the electric field contribution broadening the region of growth (not shown).

[31] While we can conclude from the above that the undulating vertical electric field and the zonal wind both play a key role in the growth rate, we cannot from this reach the conclusion that the E_s layer will be seen at the height where the growth rate reaches its peak. We must first consider the contribution of the advection term $-V_{iz}\partial n/\partial z$. This matters because the downward drift is of the order of 50 m/s throughout half of the region. With the main region of growth being of the order of 5 km only in that region of fast downward motion, an emerging layer would only have 100 s to grow, which is not enough for a growth rate of the order of 10^{-2} s^{-1} to produce a local maximum. We therefore had to resort to a numerical solution of equation (9) to take advection into account.

[32] We used a method of characteristics with initial condition n being the same everywhere and with the top boundary having that same initial value at all times.

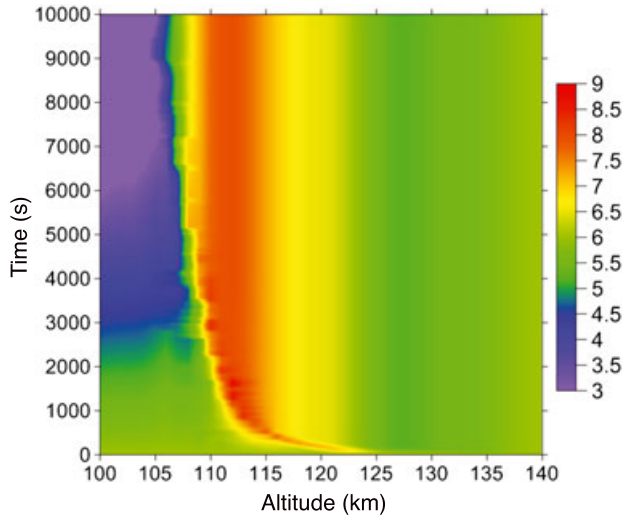

Figure 8. Example of density calculation as a function of time and altitude for the growth rates presented in Figure 7. The color scale is for $\ln n$. Given the arbitrary initial and boundary condition starting at $\ln n = 6$, only the relative values of the density matter for this plot.

In Figure 8, we show a typical result in which we specifically took $\alpha = 1$ at 128 km and had H_n equal to 3 km at 100 km altitude and growing linearly to 7 km at the top boundary at 140 km. The growth rate was arbitrarily reduced by 0.0005 s^{-1} to ensure no growth at the bottom of the simulation region. The results illustrate that the effect of the fast motion is to push the emerging E_s layer to a bottom edge where the velocities have become very small and the growth rate is going down.

[33] One difficulty with the result is that while we do indeed obtain an E_s layer, its location is well below the observed layer at 120 km. We could not change this. We could only slow down the motion of the layer by moving the $\alpha = 1$ height higher up or by changing the scale height variation, which only changed the magnitude of the growth rates in minor fashion. The only explanation we can come up with for a lower E_s layer than observed is a time-dependence effect. The electric field profile must have been changing with time. In fact, as suggested by the data themselves, there was reason to expect a connection between the position in the peak of the upper layer and the position of the minimum in the electric field (see below). Such a situation would imply that the region of decaying rates just below the peak in the E_s layer might have been moving with the layer, thereby giving the layer a higher altitude in the end by slowing its downward evolution.

[34] A final comment is in order regarding the lower E_s layer at 107 km. At that height, the vertical ion drift is so slow that a local rate calculation might be justified. In fact we can easily see that a strong shear in the wind was present at 107 km. Taking out the influence of the meridional wind because of the very small dip angle, we are left with the layer being produced by a zonal wind shear, as is usually assumed for these altitudes. We note that the growth rate inferred from the wind observations was of the order of 0.001 s^{-1} (not visible in Figure 7), meaning that it would take the order of a few 1000 s, say 1 or 2 h, to grow to a large magnitude. It may be that the region of shear might have been going down (possibly through a tidal motion) with faster growth indicated at earlier times.

[35] There remains the undulation uncovered in E_v/B and which affected the evolution of the upper E_s layer, as discussed above. A likely mechanism for this undulation and the fact that it does not involve a change in the sign of the vertical field is that the vertical field was most likely produced by the nighttime *F* region dynamo. In that case, when the *E* region conductivities are small, the *F* region dynamo is in full control and the vertical electric field tends to take the value $\mathbf{E}_v = -\mathbf{V}^F_{nx} \times \mathbf{B}$, where $\mathbf{V}^F_{nx}$ is the *F* region zonal wind and normally flows to the east in the evening sector. However, once a E_s layer has started to grow, particularly around the region $\alpha = 1$, the *E* region conductivity increases and starts to weaken the vertical field in the part of the *F* region that maps to the E_s layer. Conversely, this should also make E_v stronger in *E* region density depletion regions. This will be the case provided the zonal derivatives are weak in the *F* region, so that $\nabla \cdot \mathbf{J} \approx \partial J_z/\partial z \approx 0$ between the *E* and *F* regions, meaning that the product $E_v \Sigma_p$ is approximately constant across the E_s layer. Thus, when the *E* region contribution to Σ_p is strong, the vertical electric field should be weaker and vice versa, as observed.

4.2. The Electron Temperature Undulations and What They Reveal About the Electron Drift

[36] The anticorrelation between T_e and n_e is very clear. The temperature variation cannot be explained by adiabatic heating or cooling since the temperature is warmer in the smaller density regions. The data suggest something closer to a heat capacity effect instead, in the sense that, if there was a sustained heat source in the electron gas irrespective of the electron density, we would indeed expect to have larger temperatures in smaller density regions and vice versa.

[37] Based on high-latitude work, it would be hard to imagine that the undocumented heating source would be plasma waves. Even with rather strong Farley-Buneman turbulence at high latitudes, it is difficult to have the electron temperature reach 1000 K. In the case discussed here, the ambient electric field is much too weak to produce the kind of strong turbulence that is observed at high latitudes. We likewise have to reject solar radiation and electron precipitation as potential heat sources for the simple reason that the *E* region is in the dark and based on the low-latitude location.

[38] In work related to heating by low-frequency plasma waves [*St.-Maurice and Laher*, 1985; *Dimant and Milikh*, 2003] as well as in high-latitude electrodynamical studies [*Kagan and St.-Maurice*, 2005], anomalies in the electron temperature are obtained when large thermal electron drifts are present. In the cited work, the electron drift is produced by stronger-than-expected electric fields parallel to the geomagnetic field. In view of the success of that work, we used a similar approach here. We attributed the elevated electron temperatures to a drift of the thermal electrons along the geomagnetic field lines. The origin of such drifts is another matter and is discussed in the next subsection.

[39] We retrieved the thermal parallel electron drift by balancing the electron frictional heating term with the cooling rate resulting from collisions with the neutrals, that is,

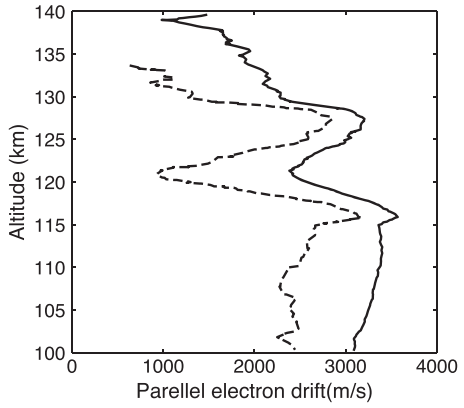

Figure 9. Magnitude of parallel electron drift derived assuming that the elevated electron temperatures were caused by frictional heating. Full line: with T_n given by MSIS. Dashed line: with T_n increased by 125 K above MSIS.

we obtained the magnitude of the parallel thermal electron velocity by solving the equation

$$\nu_{en} n_e m_e u_{e\|}^2 = C_e(T_e, T_n) \tag{12}$$

where the left-hand side represents frictional heating, with ν_{en} as the (elastic) momentum transfer collision frequency of electrons with neutrals, m_e is the electron mass, and $u_{e\|}$ is the electron drift along the geomagnetic field. The cooling rate C_e includes elastic collisions with the neutrals and, more importantly, cooling through inelastic collisions [*Schunk and Nagy*, 2009]. In the *E* region this involves mostly loss of electron energy through the excitation of fine structure of O and cooling through rotational excitation of N_2 and O_2 molecules.

[40] The result of our computation of the parallel electron drift profile is presented in Figure 9. While we could not determine the direction of the drift, it would appear that it did not change sign, at least not on the scales that we could resolve with the observations. If the drift had undergone a reversal, the magnitude should have approached zero in the vicinity of said reversal. A first result of the calculation is that the electron drift was of the order of 2.5 to 3 km/s below 130 km, with a somewhat smaller value in the middle of the E_s layer and a somewhat larger value in the strongest density depletion regions. The reason we obtained a sustained value above 2.5 km/s throughout is that T_e was well above the values expected for the neutral temperature everywhere, implying heating by friction throughout the entire *E* region. However, a source of uncertainty with the calculations is the neutral temperature itself, which we had to infer from the empirical MSIS model and could have been underestimated, meaning that we might have overestimated the frictional heating rate. We therefore repeated our calculation after raising the neutral temperature by 125 K over the MSIS model value. Interestingly, the resulting inferred parallel electron drifts were not that much smaller, retaining values that remained on the order of 2 km/s everywhere below 130 km altitude, except near 120 km.

[41] In Figure 10, we have computed the magnitude of the current density resulting from a calculation of the product $n_e q_e u_{e\|}$, using the measured electron densities and the parallel velocities retrieved from the electron frictional heating balance. An interesting point is that while the velocities are smaller around the E_s layers, the current densities are actually larger because of the larger densities involved. In particular, the current densities could reach 10 to 20 μA m^{-2} around the lower E_s layer.

4.3. Origin of the Parallel Electron Drift

4.3.1. Ambipolar Diffusion Revisited

[42] Electron motion along the magnetic field is normally neglected in the handling of diffusion equations. Given the fact that we have inferred electron drifts of the order of 2 to 3 km/s, we had to revisit the momentum balance by including electron motion as well as ion motion along the magnetic field lines so as to properly understand the role of the additional parallel electric fields and currents in the system. In particular, we could no longer assume the electron pressure gradient to be in equilibrium with the polarization electric field, and we needed to asses how this affected our understanding of the system.

[43] Using the symbol $\partial/\partial s$ for derivatives along the magnetic field, we have for the steady state electron momentum balance

$$u_{e\|} = -\frac{1}{\rho_e \nu_{en}} \frac{\partial p_e}{\partial s} - \frac{eE_\|}{m_e \nu_{en}} \tag{13}$$

where ρ_e is the electron mass density, e is the magnitude of the electronic charge, and p_e is the electron partial pressure, itself equal to $n_e K_b T_e$, where K_b is the Boltzmann constant. In this equation, the effects due to the nonlinear acceleration term and gravity were considered negligible. Next, we can obtain the electric field from the ion momentum balance written in the form

$$eE_\| = m_i g_\| + \frac{m_e}{\rho_e} \frac{\partial p_i}{\partial s} + m_i \nu_{in} u_{i\|} \tag{14}$$

where $g_\|$ is the magnitude of the component of the gravitational acceleration along the magnetic field and m_i and m_e are the ion and electron masses, respectively.

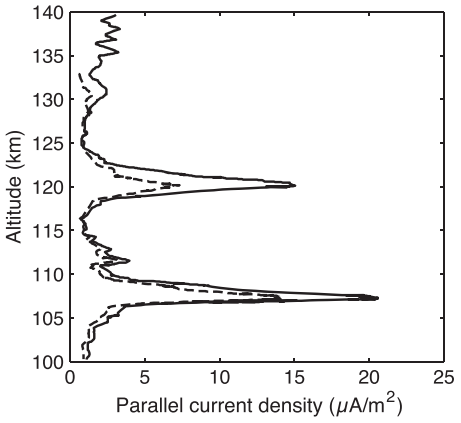

Figure 10. Parallel current density profile calculated by assuming that the elevated T_e is due to frictional heating related to a parallel electric field-induced thermal electron drift. Differences between dashed and full lines are the same as those in Figure 9.

[44] Eliminating the parallel electric field contribution by combining the above two equations, we arrive at

$$u_{i\|} + \frac{m_e}{m_i}\frac{\nu_{en}}{\nu_{in}}u_{e\|} = -\frac{K_b T_p}{m_i \nu_{in}}\left[\frac{\partial \ln(p_e + p_i)}{\partial s} + \frac{1}{H_p}\right] \qquad (15)$$

where $H_p = K_b T_p / m_i g_\|$ is the plasma scale height along the magnetic field, and $T_p = T_e + T_i$ is the plasma temperature.

[45] At this point we find that the system is not closed. Summing the ion and electron continuity equations after multiplying by the charge of each gives us the current continuity equation. With the safe assumption that the ionospheric plasma is quasi-neutral over time scales of fractions of second and longer, we obtain a second equation, which is the current continuity equation $\nabla \cdot \mathbf{J} = 0$, where $\mathbf{J}$ is the current density. The only way to close the system is to solve that equation with proper boundary conditions. From that, we can figure out the relative drift between ions and electrons. We still have to assume something about the ion or electron drift to close the system, as the currents only tell us about the relative drift. Following standard procedure, we can assume $u_{i\|} << u_{e\|}$ owing to the much smaller inertia of electrons along the magnetic field line and owing to the fact that, in the *E* region, the ion collision frequency is so high that they will not move substantially in response to parallel electric fields. This leads to the conclusion that equation (15) can be interpreted in terms of a pressure gradient which would be modified by a parallel electron drift. For $\nu_{en}/\nu_{in} \approx 10$ and an ion mass of 30 to 50 amu, $u_{e\|} = 3$ km/s would approximately be equivalent to a 3 to 5 m/s parallel ion drift in the *E* region. In other words, a 3 km/s electron drift would not create large departures from diffusive equilibrium.

[46] Having put to rest the role played by kilometer per second parallel electron drifts in the momentum balance, we can now focus on the origin of the parallel electron drifts and attendant currents through an investigation of $\nabla \cdot \mathbf{J} = 0$. We take the approach that parallel currents can be obtained from the divergence of the currents perpendicular to the magnetic field and use information from the data set at hand to estimate the perpendicular current divergence around the E_s layers, taking advantage of the plasma density, perpendicular electric field and neutral wind information. This leads us to conclude that the currents seen around the E_s layer in Figure 10 are consistent with the recorded densities, neutral winds, and electric fields. We are also led to infer that the currents in the *E* region troughs are actually produced by a different process, namely currents generated near the bottom of the *F* region at the equator through the nighttime *F* region dynamo.

4.3.2. Local Generation of Parallel Currents Around the E_s Layers

[47] To calculate the parallel currents, we need the divergence in the perpendicular currents. We already studied the ion part of the vertical currents earlier in this work. This is all we need for the ion current divergence calculation, as long as the zonal derivatives can be considered small compared to the vertical derivatives. There is also a second part to the vertical currents, namely Hall currents carried by electrons. The latter simply involves the product of the plasma density with the vertical component of the $\mathbf{E} \times \mathbf{B}$ drift, namely E_x/B. In computing the current divergence from this contribution, care must be taken not to include the $\partial E_x/\partial z$ term however, since the electric field should be curl-free, so that any contribution from this term would be balanced by a similar $\partial E_y/\partial x$ contribution.

[48] Since we had all the electric field, wind, and density terms on hand, we were able to compute the total perpendicular currents. Any divergence from these currents had to be equal to $-\partial J_\|/\partial z$, which had to be carried by thermal electrons, as explained in the previous subsection. The Hall, Pedersen, and total vertical perpendicular currents that were obtained from the data are shown in Figure 11a. It is interesting to note that the Pedersen and Hall currents tend to cancel in the upper layer but not in the bottom layer, where the currents are almost exclusively Hall currents. This, however, should not be surprising since the Pedersen ion drift is quite small in the bottom layer, owing to $\alpha >> 1$ there. This leaves the Hall currents as the only contributor to currents.

[49] The more important calculation for the determination of parallel currents is that of the divergence of the vertical currents, which should give us the divergence of $J_\|$ along the geomagnetic field. This vertical current divergence is presented in Figure 11b. A grid was added to this plot to help with a rough determination of the vertical currents based on that plot. Clearly, the divergence of the currents is controlled by the Hall currents occurring in the E_s layers, owing to the large gradient in the Hall conductivity due to the large density gradient, which changes sign on each side of the peaks. To estimate the ensuing parallel currents, consider the equation

$$\frac{\partial J_\|}{\partial y'} = -\frac{\partial J_{z'}}{\partial z'} \approx -e\frac{E_x}{B}\frac{\partial n}{\partial z'} \qquad (16)$$

Here the coordinates have been rotated through the angle I from the (y, z) to the (y', z') system so as to properly align the y' direction with the magnetic field direction, roughly 5° off the horizontal. Integrating from, say, the center of an E_s layer upward and taking the inclination into account then yields the estimate

$$\Delta J_\| = -\int \frac{\partial J_{z'}}{\partial z'}\mathrm{d}y' = -\int \frac{\partial J_{z'}}{\partial z'}\frac{\mathrm{d}y'}{\mathrm{d}z'}\mathrm{d}z' \approx \cot I \Delta J_{z'} = \frac{\Delta J_z}{\sin I} \approx 13\Delta J_z \qquad (17)$$

It is interesting to note that while there is a lack of symmetry in the contributions from the bottom versus the top parts of the layers, the integrals appear to roughly cancel, meaning that there is only a weak net parallel current left away from the layers. In the layers themselves, it can be seen from Figure 11 that the amplitude is modulated by approximately 10 μA m^{-2}. If we assume the currents to be small outside the layer, this produces a number that is in rather good agreement with the determination that we had done from the electron temperature analysis.

[50] Our main conclusion at this point is that the E_s layers must bear parallel currents because they introduce a divergence in the Hall currents, which are nearly vertical. The lower the E_s is, the more intense the fluctuations in the parallel current densities must be. However, a determination from the observations of the current divergence outside the two major E_s layers themselves is far more tentative and has not been pursued further here. For one thing we note some undulations in the current divergence in Figure 11 in association with secondary layers of ionization. The magnitudes of the oscillation are such that what would come out of the calculations should not be trusted quantitatively.

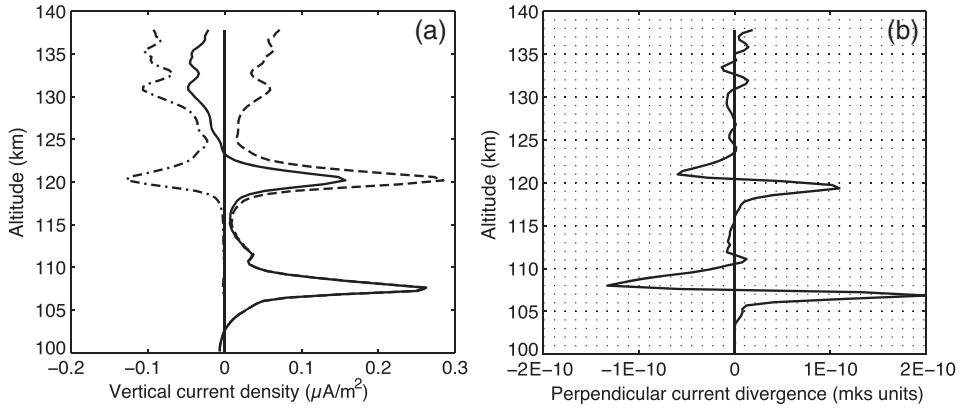

Figure 11. Profiles of vertical current density and its divergence computed from the electric field, wind, and density data. (a) Dash-dotted trace - Pedersen current density; dashed-dashed trace - Hall current density; solid trace - total vertical current density. (b) Derivative of the vertical current density.

More importantly, our results are quantitatively sensitive to our choice of altitude for $\alpha = 1$, which can only be guessed at. Also, integrating the current divergence over tens of kilometers in altitude to determine a background parallel current would amount to stating that the latitudinal extent of the layer would be ten times larger (through the $1/\sin I$ factor and uniform conditions as function of latitude). It is far from clear that this should be the case. We therefore needed to take a different approach for an explanation of the background μA/m^2 current density that was inferred from the hot electrons on each side of the major upper E_s layer.

4.3.3. Parallel Currents Generated by the *F* Region Dynamo

[51] We already discussed the presence of the *F* region nighttime dynamo when bringing out the undulation of the vertical electric field in relation to the fluctuating *E* region densities. Assuming no significant potential drop associated with parallel electric fields, the dynamo drives a current density $\Sigma_p^F V_{nx}^F B$, which has to be balanced by $(\Sigma_p^E + \Sigma_p^F)E_\perp$. If, instead of integrating over a whole field line, we integrate only the *F* region part of the dynamo, we obtain a parallel current given by

$$|\Delta J_\parallel^F| \approx |-E_\perp \frac{\partial \Sigma_p^F}{\partial z}| \approx |E_\perp| \left[n_e q_e \frac{\nu_i}{\Omega_i} \frac{\Delta s}{H} \right] \qquad (18)$$

where Δs is the length covered by the *F* region plasma in the integrated conductivity expression, and H is a scale that corresponds to either the neutral scale height or to the bottomside rate of increase in the *F* region electron density. If we assume no current above the *F* region peak, $\Delta J_\parallel^F$ becomes the current density just below the *F* peak.

[52] With $\Delta s/H$ of order 30, $E_\perp/B$ of the order of 50 to 100 m/s and an *F* peak density of the order of 10^{11} m^{-3}, we obtain a parallel current density of the order of 1 to 2 μA m^{-2}. If the dynamo field is to be affected by the *E* region densities (as observed), then this current has to extend, through geomagnetic field lines, all the way to the bottom of the *E* region. This requires the divergence of the Pedersen currents to be small along the vertical direction, away from the *E* region source itself. But it so happens that, in the trough regions, the conductivities go through a minimum while the vertical (zonal) electric field also goes through a minimum at the same place (as indicated by the observations). Thus, the trough regions, at least at *E* region altitudes, are regions which are essentially free of Pedersen current divergence, meaning that parallel currents could indeed be maintained away from their source region, as expected from the observed modulation of the *F* region dynamo field by the *E* region density.

[53] Our 1 to 2 μA m^{-2} current density estimate turns out to be comparable to what we had derived from the elevated electron temperatures between the E_s layers, strongly suggesting that parallel currents triggered by the *F* region dynamo are indeed responsible for the very large electron temperatures observed in the density minima regions. It is interesting to note, therefore, that the *F* region nighttime dynamo affects parallel current densities and electron temperature in the *E* region through two different mechanisms: around the E_s peaks, the zonal electric field arising from the *F* region dynamo forces large changes in parallel current densities to be triggered across the layers. In the broader troughs, the parallel current densities are weaker and originate near the bottom of the *F* region dynamo itself rather than in the *E* region. Ironically in this latter case, the current

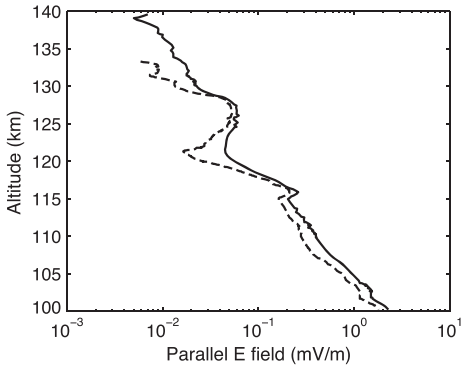

Figure 12. Parallel electric field profile calculated by assuming that the elevated T_e is due to frictional heating due to a parallel electric field-induced thermal electron drift. Differences between dashed and full lines are the same as those in Figure 9.

densities are weaker by one order of magnitude even though they produce much larger electron temperatures, because the much weaker densities require much larger velocities for the parallel current to be carried.

[54] For completeness we have computed the parallel electric field through the observation region from the parallel currents obtained by our frictional heating method. The result is presented in Figure 12. Aside from going through undulations around the E_s layers, the parallel electric field essentially decreases exponentially with altitude.

5. Summary and Conclusions

[55] For the EQUIS-II rocket campaign, we have obtained high resolution electron temperature and density profiles from sweeping Langmuir probe measurements. As the derived plasma densities from the Langmuir probe measurements match very well with absolute density measurements from plasma impedance probe, we have high confidence in our observations. Thus, we have shown that it is possible to use sweeping Langmuir probe data even when the spacecraft surface-to-probe area ratio is smaller than 1000. Our observations have confirmed the results from previous investigations of the *E* region after sunset, showing that the electron temperature can increase dramatically above or below a strong E_s layer.

[56] In the particular flight that we analyzed in detail, two E_s layers of comparable density peaks were observed, with two regions of elevated electron temperatures on both sides of the upper E_s layer near 120 km altitude. Using the observed neutral wind profile and the observed electric fields, we were able to establish that while the lower E_s layer was apparently associated with a zonal wind shear, as would normally have been expected, the upper E_S layer was a far more complicated matter that resulted from the combined action of undulations in the vertical electric field, shears in the zonal wind, altitude variations in the collision frequency, and a strong downward advection term. We still could not match the altitude of the upper layer, which we speculated might have been due to changing electric field conditions in response to the presence of the E_s layer itself.

[57] Assuming the elevated electron temperatures to be due to electron frictional heating in the presence of parallel currents, we inferred that parallel current densities of the order of 10 μA m^{-2} were flowing on each side of the E_s peaks while parallel current densities of the order of 1 to 2 μA m^{-2} were flowing around the density troughs. Ironically, the smaller current densities of the troughs were associated with much larger electron temperatures because of the depleted number of current carriers.

[58] Using the observed wind and electric field values, we showed that the parallel current densities inferred from electron frictional heating calculations were consistent with those inferred from the perpendicular electric fields. The *F* region dynamo downward/southward component of the electric field was responsible for the parallel currents in both cases, though through different mechanisms. In the instance of the E_s layer itself, the *E* region Hall currents introduced by the dynamo field had to diverge because of the large density changes. In the case of the troughs, there was little current closure through most of the *E* region and the smaller parallel currents generated at the base of the *F* region dynamo in the equatorial region therefore had to extend deep into the *E* region. This conclusion is consistent with the observed modulation of the dynamo field by *E* region densities.

[59] Our explanation for the anticorrelation between *E* region electron temperatures and the electron densities is new and lends itself to further studies. Of particular interest is the fact that we have found that the largest observed electron temperatures were not related to the largest parallel current densities in the system. Rather, the temperatures were elevated because rather weak parallel currents had to introduce large electron drifts if the number of charged carriers was small. This observation might be relevant for a study of *E* region electron temperatures in situations observed elsewhere in the past, where very small (a few 1000 cm^{-3}) densities were usually accompanied by distinctly high electron temperatures [*Oyama et al.*, 2008a], only to go down wherever the density was going up (in E_s layers for instance). In the light of the present work, these observations suggest that there might be small field-aligned currents circulating between the *E* and *F* region pretty much at all times of the night and that the electron temperature could be used as a tool to monitor the strength of said parallel current densities. The method could be extended to larger nighttime plasma density situations if only there could be a better way to compare electron and neutral temperatures. This would allow the study of parallel currents to be extended to more situations and allow for a more thorough study of parallel currents induced around the E_s layers themselves, where the current densities may be higher and yet the temperature enhancements have to be smaller.

[60] **Acknowledgments.** Jean-Pierre St-Maurice's work was supported by funding from NSERC, and a Canada Research Chair at the University of Saskatchewan.

[61] Robert Lysak thanks the reviewers for their assistance in evaluating this paper.

References

Amatucci, W. E., P. W. Schuck, D. N. Walker, P. M. Kintner, S. Powell, B. Holbeck, and D. Leonhardt (2001), Contamination-free sounding rocket Langmuir probe, *Rev. Sci. Instrum.*, *72*(4), 2052–2057.

Barjatya, A., and C. M. Swenson (2006), Observations of triboelectric charging effects on Langmuir-type probes in dusty plasma, *J. Geophys. Res.*, *111*, A10302, doi:10.1029/2006JA011806.

Barjatya, A. (2007), Langmuir probe measurements in the ionosphere, PhD Dissertation, Utah State University Institutional Repository: Graduate Theses and Dissertations 2007-05-01 Utah State University - Merrill-Cazier Library. paper 274 http://digitalcommons.usu.edu/etd/274.

Barjatya, A., C. M. Swenson, D. C. Thompson, and K. H. Wright Jr. (2009), Invited article: Data analysis of the floating potential measurement unit aboard the international space station, *Rev. Sci. Inst.*, *80*, 041,301, doi:10.1063/1.3116085.

Bekkeng, T. A., A. Barjatya, U. P. Hoppe, A. Pederson, J. I. Moen, M. Friedrich, and M. Rapp (2013), Payload charging events in the mesosphere and their impact on Langmuir type electric probes, *Ann. Geophys.*, *31*, 187–196, doi:10.5194/angeo-31-187-2013.

Brace, L. H. (1998), Langmuir probe measurements in the ionosphere, in *Measurement Techniques in Space Plasmas: Particles, Geophysical Monograph Series,* vol. 102, edited by R. F. Pfaff, J. E. Borovsky, and D. T. Young, pp. 23–35, AGU, Washington, D.C.

Chen, F. F. (1965), Electric probes, in *Plasma Diagnostic Techniques*, edited by R. Huddlestone, and S. Leonard, pp. 113–200, Academic Press, New York.

Dimant, Y. S., and G. M. Milikh (2003), Model of anomalous electron heating in the *E* region: 1. Basic theory, *J. Geophys. Res.*, *108*(A9), 1350, doi:10.1029/2002JA009524.

Friedrich, M., K. M. Torkar, U. P. Hoppe, T. A. Bekkeng, A. Barjatya, and M. Rapp (2013), Multi-instrument comparisons of *D*-region plasma measurements, *Ann. Geophys.*, *31*, 135–144, doi:10.5194/angeo-31-135-2013.

Haldoupis, C., D. Pancheva, and N. J. Mitchell (2004), A study of tidal and planetary wave periodicities present in midlatitude sporadic *E* layers, *J. Geophys. Res.*, *109*, A02302, doi:10.1029/2003JA010253.

Hysell, D. L., M. F. Larsen, C. M. Swenson, A. Barjatya, T. F. Wheeler, M. F. Sarango, R. F. Woodman, and J. L. Chau (2005), Onset conditions for equatorial spread *F* determined during EQUIS II, *Geophys. Res. Lett.*, *32*, L24104, doi:10.1029/2005GL024743.

Hysell, D. L., M. F. Larsen, C. M. Swenson, and T. F. Wheeler (2006), Shear flow effects at the onset of equatorial spread *F*, *J. Geophys. Res.*, *111*, A11317, doi:10.1029/2006JA011963.

Kagan, L. M., and J. P. St.-Maurice (2005), Origin of type-2 thermal-ion upflows in the auroral ionosphere, *Ann. Geophys.*, *23*, 13–24, doi:10.5194/angeo-23-13-2005.

Oyama, K. I. (1976), A systematic investigation of several phenomena associated with contaminated Langmuir probes, *Planet. Space Sci.*, *24*, 183.

Oyama, K. I., C. H. Lee, H. K. Fang, and C. Z. Cheng (2008a), Means to remove electrode contamination effect of Langmuir probe measurement in space, *Rev. Sci. Inst.*, *83*, 055,113, doi:10.1063/1.4722167.

Oyama, K. I., T. Abe, H. Mori, and J. Liu (2008b), Electron temperature in nighttime sporadic *E* layer at mid-latitude, *Ann. Geophys.*, *26*, 533–541.

Schunk, R. W., and A. F. Nagy (2009), *Ionospheres: Physics, Plasma Physics, and Chemistry (Cambridge Atmospheric and Space Science Series),* 2nd ed., Cambridge Univ. Press, Cambridge, U. K.

Steigies, C. T., and A. Barjatya (2012), Contamination effects on fixed bias Langmuir probes, *Rev. Sci. Inst.*, *83*, 113,502, doi:10.1063/1.4764582.

St.-Maurice, J.-P., and R. Laher (1985), Are observed broadband plasma wave amplitudes large enough to explain the enhanced electron temperatures of the high-latitude *E* region?, *J. Geophys. Res.*, *90*(A3), 2843–2850, doi:10.1029/JA090iA03p02843.

Szuszczewicz, E. P. (1972), Area influences and floating potentials in Langmuir probe measurements, *J. Appl. Phys.*, *43*(3), 874.

Tsunoda, R. T. (2008), On blanketing sporadic *E* and polarization effects near the equatorial electrojet, *J. Geophys. Res.*, *113*, A09304, doi:10.1029/2008JA013158.